



Synergistic induced charge transfer switch by oxygen vacancy and pyrrolic nitrogen in $\text{MnFe}_2\text{O}_4/\text{g-C}_3\text{N}_4$ heterojunctions for efficient transformation of bicarbonate to acetate in photo-assisted MES

Weifeng Kong^a, Liping Huang^{a,*}, Xie Quan^a, Gianluca Li Puma^{b,*}

^a Key Laboratory of Industrial Ecology and Environmental Engineering, Ministry of Education (MOE), School of Environmental Science and Technology, Dalian University of Technology, Dalian 116024, China

^b Environmental Nanocatalysis & Photoreaction Engineering, Department of Chemical Engineering, Loughborough University, Loughborough LE11 3TU, United Kingdom

ARTICLE INFO

Keywords:

Microbial electrosynthesis
Photocatalysis
Charge transfer switching
Oxygen vacancy
Pyrrolic nitrogen

ABSTRACT

Inorganic carbon (HCO_3^-) was efficiently converted into acetate (204.4 ± 0.5 mM with a coulombic efficiency of $96 \pm 3\%$ over 24 days operation) in a photo-assisted microbial electrosynthesis system (MES) using a urea-treated $\text{MnFe}_2\text{O}_4/\text{g-C}_3\text{N}_4$ cathode and the nonphotosynthetic bacteria *Serratia marcescens* Q1. The remarkable photocatalytic performance of $\text{MnFe}_2\text{O}_4/\text{g-C}_3\text{N}_4$ heterojunction was resulted from the charge transfer mechanism switch (from type II to Z-scheme) induced by the synergistic effect of oxygen vacancies and pyrrolic N after urea treatment. The increased pyrrolic N was conducive to photoinduced electron transfer while the oxygen vacancies provided a higher fraction of surface-active sites for H_2 evolution, which was metabolized in-situ with bicarbonate by *S. marcescens* Q1 to yield acetate via the Wood-Ljungdahl pathway. This study provides a simple and feasible strategy for switching the photocatalytic charge transfer in a spinel-based heterojunction and offers new insights for ingeniously synthesizing photocatalysts with high CO_2 conversion in MES.

1. Introduction

Photo-assisted microbial electrosynthesis systems (MES) has shown promise to achieve a sustainable carbon neutral process for efficient production of liquid fuels and value-added chemicals (e.g., acetate) from inorganic carbon reduction [1–4]. Photo-assisted MES combined photocatalytic semiconductor materials with electroactive bacteria such as InP [1], CdS [2], Si nanowires/TiO₂/Ni [4], WO₃/MoO₃/g-C₃N₄ [5], and Ag₃PO₄/g-C₃N₄ [6], has achieved efficient inorganic carbon reduction. In these systems, photo-induced holes (photooxidation) are refilled by the electrons traveling from the anode drawing a stronger circuit current, while photo-induced electrons (photoreduction) under anaerobic conditions evolve hydrogen (indirect H₂ mediator). Both electrons and H₂ are metabolized with inorganic carbon by electrotrophs to produce acetate. However, the most negative conduction band edge of these reported photocatalysts is -1.2 eV (vs. standard hydrogen electrode, SHE) [1–6], which is insufficiently negative to yield a high rate of hydrogen production. The reduction of bicarbonate to acetate is limited by the in-situ metabolic assimilation of H₂ providing indirect electron transfer to the electrotrophs [2–6]. Thus, the exploration of appropriate

photocatalysts with sufficiently more negative conduction band edges, capable of efficient H₂ production via photoreduction would likely yield efficient acetate production from inorganic carbon reduction.

Manganese ferrite (MnFe_2O_4), a well-known spinel-type semiconductor, has been considered as a promising photocatalyst due to its narrow band gap, more negative conduction band (-1.6 eV vs. SHE), high photochemical stability, cost-effectiveness, good biocompatibility and environmental friendliness [7,8]. Hybridizing MnFe_2O_4 with graphitic carbon nitride (g-C₃N₄), an environmental metal-free photocatalyst [9,10], has been shown to suppress high recombination of photogenerated electron-hole pairs, compared to the pure MnFe_2O_4 and thus enhance the photooxidative degradation of antibiotics such as metronidazole, amoxicillin, tetracycline and ciprofloxacin [7], and methyl orange dye [11]. While these studies have provided insightful information on the potential of $\text{MnFe}_2\text{O}_4/\text{g-C}_3\text{N}_4$ for the photooxidation of recalcitrant organics, the exploitation of the reductive pathway offered by photo-generated electrons in this heterojunction has been largely underestimated. More importantly, low efficiencies of the separating and the photocatalysis based on the traditional type II mechanism have largely restricted the expansion of their applications. In contrast to

* Corresponding authors.

E-mail addresses: lipinghuang@dlut.edu.cn (L. Huang), g.li.puma@lboro.ac.uk (G.L. Puma).

<https://doi.org/10.1016/j.apcatb.2022.121214>

Received 28 September 2021; Received in revised form 20 January 2022; Accepted 12 February 2022

Available online 15 February 2022

0926-3373/© 2022 Elsevier B.V. All rights reserved.

the common type II mechanism of $\text{MnFe}_2\text{O}_4/\text{g-C}_3\text{N}_4$, many other g- C_3N_4 -based hybrids such as $\text{Ag}_3\text{PO}_4/\text{g-C}_3\text{N}_4$ [12], $\text{CdS}/\text{g-C}_3\text{N}_4$ [13], $\text{W}_{18}\text{O}_{49}/\text{g-C}_3\text{N}_4$ [14] and $\text{WO}_3/\text{MoO}_3/\text{g-C}_3\text{N}_4$ [5] have proven to form Z-scheme heterojunctions promoting either photocatalytic hydrogen evolution or acetate production from inorganic carbon reduction. However, these heterojunctions suffer intrinsic limitations related to photoreduction capability, operational stability, biocompatibility and environmental sustainability, which together have limited their practical application [15]. Considering the good properties of $\text{MnFe}_2\text{O}_4/\text{g-C}_3\text{N}_4$, it should be possible to intrinsically enhance the photoreduction catalytic performance of this heterojunction by switching operation from a common type II mechanism to a Z-scheme charge transfer pathway, thus enhancing the production of acetate from inorganic carbon reduction in photo-assisted MES. This can be engineered by introducing oxygen vacancies into the semiconductors lattice.

As an intrinsic and fundamental defect of metal oxide semiconductors, oxygen vacancies play a vital role in their physicochemical and electronic properties such as charge separation, electronic band structures and transport properties [16,17]. Oxygen vacancies in Bi_2O_3 reduce the adsorption energy of CO_2 and offer abundant localized electrons, thereby improving CO_2 photoreduction [16]. Urea-treated BiOBr yields a hierarchical microflower structure and increases the amount of defective oxygen vacancies and the rate of photocatalytic degradation of Rhodamine B dye [18]. Furthermore, Lotsch's group demonstrated that the energy levels of g- C_3N_4 could be modified by urea treatment, enabling strong photocatalyst/cocatalyst interactions and faster charge transfer [10]. Alternatively, pyrrolic N-enriched materials instead of pyridinic N and graphitic N enhances photoinduced charge transfer [19,20] and thus extracellular electron transfer processes via the improved biofilm-electrode interaction [21,22]. The extracellular electron transfer process between electrodes and cell surface is regulated by outer membrane c-type cytochromes composed of central functional porphyrin iron [2–3,21]. Pyrrolic N produced via urea treatment, presents the lowest adsorption energy and the strongest affinity with porphyrin iron compared with graphitic N and pyridine N, enabling faster uptake of electrons from c-type cytochromes [21,22]. Treatment of $\text{MnFe}_2\text{O}_4/\text{g-C}_3\text{N}_4$ with urea is therefore expected to provide supplementary oxygen vacancies and pyrrolic N sites, altering the semiconductors energy levels, and the charge transfer mechanism of $\text{MnFe}_2\text{O}_4/\text{g-C}_3\text{N}_4$ producing efficient charge carriers separation and higher rates of acetate production from inorganic carbon.

In this study, a pyrrolic nitrogen-enriched $\text{MnFe}_2\text{O}_4/\text{g-C}_3\text{N}_4$ photocathode with oxygen vacancies generated by urea treatment was developed and anaerobically operated for efficient acetate production from inorganic carbon reduction in a MES incorporating the non-photosynthetic *Serratia marcescens* Q1 electrotoph. The charge transfer of $\text{MnFe}_2\text{O}_4/\text{g-C}_3\text{N}_4$ heterojunction was switched from type II to a Z-scheme mechanism by generation of synergistic oxygen vacancies and pyrrolic N sites via urea treatment, the presence of which was demonstrated by ultraviolet photoelectron spectroscopy (UPS) and X-ray photoelectron spectroscopy (XPS). The stability and the efficiency of this hybrid photo-assisted MES were systematically assessed over 24 days continuous operation. Multiple approaches were extensively used to characterize the performance of the photocathode including X-ray diffraction (XRD), Zeta potential, photoluminescence (PL), transient photocurrent response tests, scanning electron microscopy equipped with an energy dispersive X-ray spectroscopy (SEM-EDS), ultraviolet-visible diffuse reflection spectra (UV-vis DRS), electron spin resonance (ESR), cyclic voltammetry (CV), differential pulse voltammetry (DPV) and electrochemical impedance spectroscopy (EIS). High-sensitivity flow cytometry was employed to assess the electrotophic viability under various conditions. This study demonstrates a feasible strategy to enhance the production of acetate in photo-assisted MES using inorganic carbon as feedstock.

2. Materials and methods

2.1. Synthesis of g- C_3N_4 and $\text{MnFe}_2\text{O}_4/\text{g-C}_3\text{N}_4$ powders

The synthesis of g- C_3N_4 and $\text{MnFe}_2\text{O}_4/\text{g-C}_3\text{N}_4$ was similar to the previously reported [5,7] with appropriate modification. In brief, 10 g melamine powder was calcined at 550 °C in a muffle furnace for 4 h with a heating rate of 3 °C/min. This g- C_3N_4 was then ground into powder and named as the urea-untreated g- C_3N_4 . The urea-treated g- C_3N_4 was fabricated as the above procedures by the mixture of melamine and urea.

The $\text{MnFe}_2\text{O}_4/\text{g-C}_3\text{N}_4$ powder was carried out as follows: The urea-untreated g- C_3N_4 powder was added into 50 mL deionized water and ultrasonicated for 1 h. After that, 0.132 g $\text{MnCl}_2 \cdot 9\text{H}_2\text{O}$, 0.301 g $\text{FeCl}_3 \cdot 9\text{H}_2\text{O}$ and different amounts of urea (0, 0.082, 0.164, 0.246, 0.328 g) were dissolved in the above solution by magnetic stirring for 0.5 h. Thereafter, the solution pH was adjusted to 12 with 5 M NaOH and stirred for 1 h, yielding a homogeneous emulsion. The emulsion was then transferred into a 100 mL Teflon-lined stainless steel autoclave and heated at 200 °C for 12 h. The obtained $\text{MnFe}_2\text{O}_4/\text{g-C}_3\text{N}_4$ powder was washed with deionized water and ethanol alternately after grinding, and dried at 60 °C in an oven overnight to get desired sample. Different molar ratios (4: 1, 3: 1, 2: 1, 1: 1, 1: 2, 1: 3 and 1: 4) of MnFe_2O_4 and g- C_3N_4 were obtained. The urea-treated MnFe_2O_4 was synthesized using the same procedures as mentioned above without the addition of g- C_3N_4 . All the urea-untreated controls were fabricated as the same processes of urea-treated photocatalysts without the addition of urea.

The $\text{MnFe}_2\text{O}_4/\text{g-C}_3\text{N}_4$ photocathode was prepared according to the description in Supporting Information (SI).

2.2. Reactor construction, electrotoph inoculation and operation

The dual-chamber MES reactor was similar to previously reported [6]. The above prepared $\text{MnFe}_2\text{O}_4/\text{g-C}_3\text{N}_4$ electrode was employed as cathode, whereas a saturated calomel electrode (SCE, +241 mV versus SHE) served as cathode reference electrode and a carbon rod was used as anode. All electrode potentials were reported versus SHE unless otherwise mentioned.

The anode chamber was inoculated with suspended bacteria from acetate-fed microbial fuel cells and fed by nutrient solution with equivalent volume as previously described [23–25]. The cathode chamber was inoculated with *Serratia marcescens* Q1, a non-photosynthetic electrotoph and capable of metabolizing inorganic carbon to acetate [5,6]. The catholyte was composed of NaHCO_3 (23.8 mM), NH_4Cl (2.1 mM), KH_2PO_4 (0.09 mM), mineral 0.6 mL/L and vitamins 0.6 mL/L. The initial catholyte pH was adjusted to 5.8 [5,6] whereas the amount of the *S. marcescens* Q1 inoculation in the catholyte was a final OD_{600} of 0.35 [1,5–6]. This catholyte was then sparging with pure N_2 gas for 15 min in an anaerobic glovebox (YQX-II, Xinmiao, Shanghai) before fed into the MES. The cathode was poised at a potential -1.1 V (vs. SHE) and the light intensity of 26.9 kLux (via a 100 W iodine tungsten lamp) were used as previously described [5–6,26]. The temperature of all the reactors was kept at 25 ± 3 °C [26]. All the data were recorded after the first operational cycle and the operation was triplicate at least [5].

Four control experiments were conducted: a) the urea untreated control, which elucidated the impact of urea treatment on this MES performance; b) the abiotic control, which reflected the impact of the electrotoph on the metabolism of inorganic carbon and H_2 ; c) the no light control, which established the role of light irradiation in the photocathode process; d) the fourth control investigated the roles of the $\text{MnFe}_2\text{O}_4/\text{graphite}$ felt, the g- $\text{C}_3\text{N}_4/\text{graphite}$ felt and the bare graphite felt in the photocatalytic performance.

2.3. Characterizations and electrochemical measurements

The morphologies and structure of the photocathodes with or without biofilms were characterized by SEM (Nova NanoSEM 450, FEI company, USA) equipped with EDS (X-MAX 20–50 mm², Oxford Instruments, UK) and XRD (XRD-6000 using Cu K α radiation, Shimadzu, Japan). The chemical components and binding energy change were studied by XPS (ESCALAB250, Thermo, USA). The PL measurements were examined by a fluorescence spectrophotometer (F-4500, Hitachi, Japan) with an excitation wavelength of 325 nm. The photocurrent response measurements were recorded in 0.1 M Na₂SO₄ electrolyte under light illuminance. The UV–vis DRS spectra of the semiconductor photocatalysts were recorded with a Lambda 750 S UV–vis spectrophotometer. Zeta potential was analyzed on Zetasizer Nano ZS90. The ESR measurements were carried out on a Bruker A200 (Karlsruhe, Germany). The Brunauer–Emmett–Teller (BET) surface area was investigated with N₂ adsorption-desorption curve by Quadrasor-SI (Quantachrome, USA). CV and DPV were conducted with a potentiostat (BioLogic, VSP, France) at a slow scan rate of 0.1 mV/s. EIS was determined at the frequency range of 0.01–100 kHz with an amplitude of 5 mV at –1.1 V versus SHE, where a Zsimpwin software was employed to acquire the equivalent circuit and different resistances values [26,27]. The work function (Φ) of sample was determined using UPS (ESCALAB250, Thermo, USA) with He I energy. Φ , E_F , conduction band edge potential (E_{CB}) and valance band edge potential (E_{VB}) of single photocatalyst with or without urea treatment were calculated from the UPS (Eqs. (1)–(3)) [28,29]:

$$\Phi = -E_F = h\nu - E_H \quad (1)$$

$$E_{VB} = -(h\nu - E_H + E_L) \quad (2)$$

$$E_{CB} = E_{VB} - E_g \quad (3)$$

where $h\nu$ is the excitation energy of 21.22 eV, and the high kinetic energy cutoff (E_H) and low kinetic energy cutoff (E_L) were estimated according to the tangent lines in each region. All the above calculated energy levels were referred to the vacuum level (E_{abs}). According to the relationship between the E_{abs} and the standard hydrogen electrode (E_{SHE}), $E_{abs} = -E_{SHE} - 4.44$ (at 25 °C) [28], all the results were converted to values versus SHE and summarized in Table 1.

2.4. Analysis and calculations

The gas chromatograph (GC7900, Tianmei, China) was employed to measure the concentration of acetate in catholyte and the residual hydrogen in the cathodic headspace, and the values of H₂ were normalized to the catholyte volume and operational time (m³/m³/d). SE-54 cross-linking chromatographic column and thermal conductivity detector were used for hydrogen determination using N₂ as the carrier gas. The temperatures of the column and the injector were both 120 °C. For acetate measurement, PEG-20M column and flame ionization detector were employed using nitrogen as the carrier gas. The temperatures of the column and the injector were both 200 °C. The concentration of inorganic carbon in the catholyte was measured by the

Table 1

Energy levels of single MnFe₂O₄ and g-C₃N₄ with or without urea treatment calculated from UV–vis DRS and UPS data.

	MnFe ₂ O ₄ -urea	g-C ₃ N ₄ -urea	MnFe ₂ O ₄ -no urea	g-C ₃ N ₄ -no urea
Φ (eV)	3.68	3.75	4.22	3.71
E_F (eV)	-0.76	-0.69	-0.22	-0.73
E_H (eV)	17.54	17.47	17.00	17.51
E_L (eV)	0.73	2.36	0.30	2.31
E_g (eV)	1.62	2.56	1.58	2.61
E_{VB} (eV)	-0.03	1.67	0.08	1.58
E_{CB} (eV)	-1.65	-0.89	-1.50	-1.03

national standard method (DZ/T 0064.49-93) and the consumption of inorganic carbon (%) was evaluated by the differences between the initial and the final inorganic carbon concentrations in the catholyte, divided by the initial concentration of inorganic carbon. The leached Mn and Fe in the catholyte (%) was measured by the national standard method (Fe: DZ/T 0064.23-93; Mn: DZ/T 0064.31-93), and calculated from the amounts of Fe and Mn in the catholyte divided by the initial Fe or Mn on the cathode. The electrocatalytic viability was assessed by a high-sensitivity flow cytometry (Accuri C6 Plus, BD company, USA) in the presence of the photocatalysts and light irradiation [5,6].

The long-term stability of the MnFe₂O₄/g-C₃N₄ photocathode was determined over 24 d operation with periodical supply of bicarbonate. A 1.5 mL catholyte was sampled each half-day and an equal volume of solution (170.6–183.4 mM) was replenished to maintain the initial inorganic carbon concentration of 23.8 mM. The controls were conducted by the same procedures, except that the supplementary inorganic carbon concentrations were different.

The coulombic efficiency for acetate production ($CE_{acetate}$) was obtained through Eq. (4) [3–6]:

$$CE_{acetate} = \frac{8 \times n_a \times F}{\int_0^t Idt} \times 100\% \quad (4)$$

where n_a (mol) is the acetate mole amount, F (96485 C/mole electron) is the Faraday constant, I (A) is the current, and t is the operation time (s).

The statistical significance of the data was analyzed by ANOVA in SPSS 19.0 (t-test, $p = 0.05$).

3. Results and discussion

3.1. Characterization of prepared photo-assisted cathode

The characteristic peaks in the XRD pattern (Fig. 1A) of MnFe₂O₄ were located at 17.8°, 29.8°, 35.0°, 42.7°, 53.6°, 56.2°, 62.3° corresponding to the (111), (220), (311), (400), (422), (511) and (440) crystalline facets, in good agreement with the spinel MnFe₂O₄ crystalline structure (JCPDS No.74-2403) [7]. Two diffraction peaks at 13.1° (100) and 27.3° (002) were observed in g-C₃N₄ sample [8,12]. The coexistence of both g-C₃N₄ and MnFe₂O₄ diffraction peaks in MnFe₂O₄/g-C₃N₄ XRD pattern suggested the successful combination of the two photocatalysts. Besides, all the same samples exhibited similar diffraction peaks, indicating that the crystallization and phase structure of the photocatalysts was not affected by urea treatment.

Zeta potential analysis was performed to study the superficial electrokinetic potential of the photocatalysts (Fig. 1B). The more positive zeta potential of MnFe₂O₄/g-C₃N₄ observed after urea treatment enhanced adsorption of negatively charged HCO₃[−] anions and therefore favored higher rates of acetate production.

PL analysis (Fig. 1C) and transient photocurrent response tests (Fig. 1D) were used to assess the separation efficiency of photoinduced electron-hole pairs. Whilst the pure MnFe₂O₄ phase did not report PL signal, appreciably lower PL intensities were observed with the urea treated MnFe₂O₄/g-C₃N₄, in comparison to the untreated heterojunction and g-C₃N₄ control. These results clearly demonstrated the significant role of urea treatment in decreasing the recombination of photo-generated carriers as well as promoting strong interactions between MnFe₂O₄ and g-C₃N₄, thus suppressing the recombination of photo-generated carriers. Other studies have demonstrated a similar attenuation of the PL signal in other semiconductors BiOBr [18] or BiOBr/BiOAc_{1-x}Br_x [30] after urea treatment. Under the same urea treatment, the photocurrent of the MnFe₂O₄/g-C₃N₄ (8.3 μ A) cathode increased by at least one order of magnitude in comparison to the MnFe₂O₄ (0.6 μ A) or g-C₃N₄ (0.5 μ A) (Fig. 1D) phases, and was 2.9 times higher than the untreated controls. This phenomenon was similar to the enhanced photocurrent of urea-treated BiOBr or BiOBr/BiOAc_{1-x}Br_x for degradation of Rhodamine B dye [18,30]. These results collectively

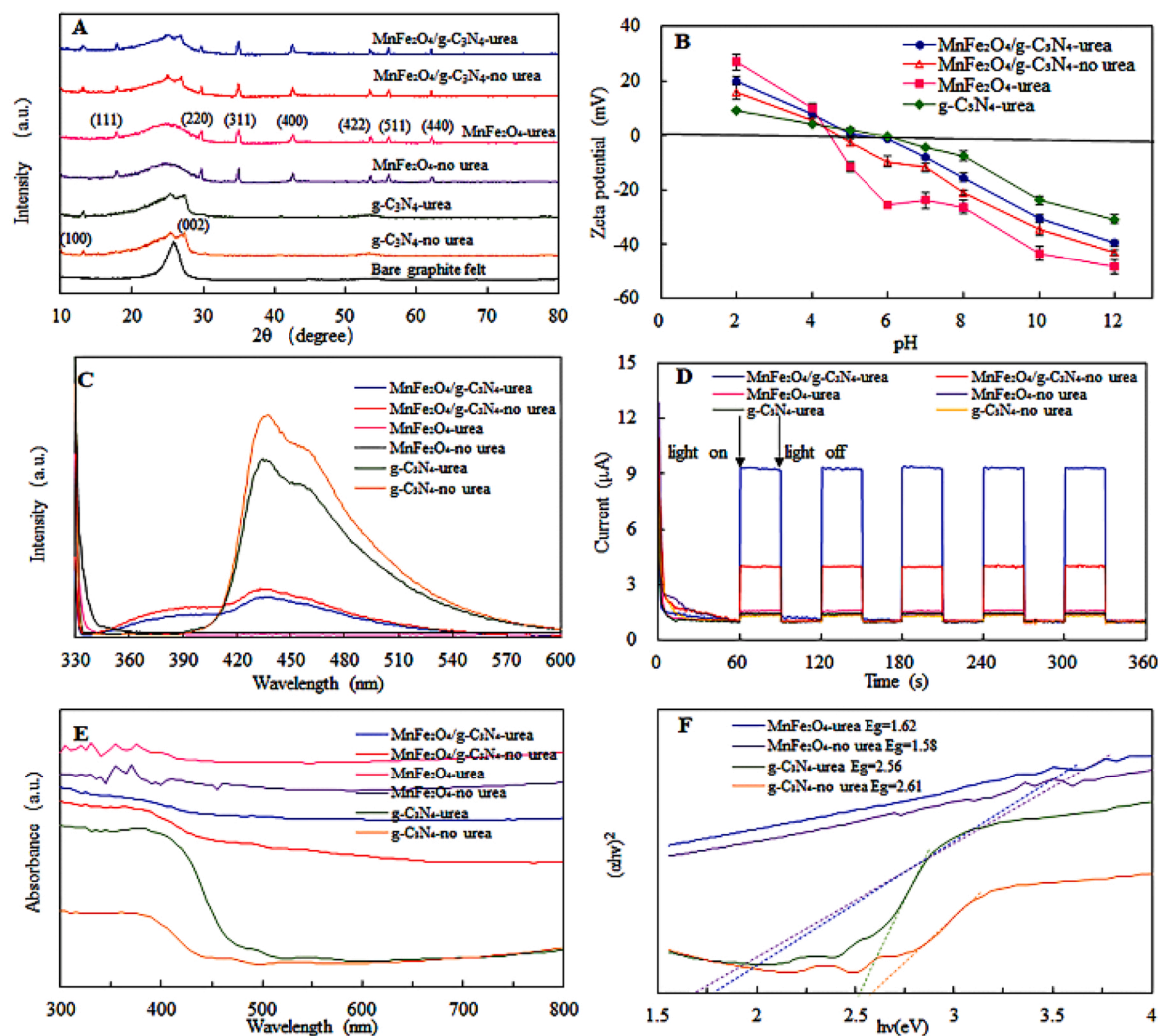


Fig. 1. XRD diffraction patterns (A), Zeta potential (B), photoluminescence spectra (C), transient photocurrent responses (D), UV-vis DRS spectra (E), and Tauc plots (F) of the cathodes with or without photocatalyst.

confirmed highly efficient charge carrier separation in this urea treated MnFe₂O₄/g-C₃N₄ heterojunction.

The optical absorption and band gaps of the semiconductor were determined by UV-vis DRS (Fig. 1E), where the urea treated g-C₃N₄ exhibited a broader absorption edge (484 nm) than the untreated control (475 nm), whereas all the MnFe₂O₄ showed broad absorption over ultraviolet and visible regions. Compared with g-C₃N₄, MnFe₂O₄/g-C₃N₄ showed similar curves apart from enhanced intensity, indicating that MnFe₂O₄ can amplify the light absorption of this heterojunction [14, 31]. The invariable stronger absorption intensity of the urea treated samples compared to the untreated controls stressed the importance of urea treatment for the enhancement of light absorption. The band gaps (E_g) of MnFe₂O₄ and g-C₃N₄ were estimated through Tauc plots (Fig. 1F; Table 1) [32]. The Mott-Schottky test (Fig. S1) was employed to determine the semiconductor type. The positive slopes in the Mott-Schottky plots of all g-C₃N₄ (Fig. S1C) verified the nature of n-type semiconductors, whereas all MnFe₂O₄ (Fig. S1B) were p-type semiconductors with negative slopes [33]. The two photocatalysts thus constructed a p-n heterojunction in the composite. Moreover, the carrier density N_D of the urea treated MnFe₂O₄/g-C₃N₄ heterojunction ($2.3 \times 10^{17} \text{ cm}^{-3}$) calculated from the Mott-Schottky curves [34], was obviously higher than the N_D obtained with either the urea-treated single phase photocatalysts (MnFe₂O₄: $6.4 \times 10^{16} \text{ cm}^{-3}$; g-C₃N₄: $6.5 \times 10^{16} \text{ cm}^{-3}$) or the untreated MnFe₂O₄/g-C₃N₄ controls ($7.0 \times 10^{16} \text{ cm}^{-3}$) (Fig. S1). This clearly suggests the utilization of a higher fraction of photoinduced charge

carriers in the urea treated heterojunction, facilitating the photocatalytic processes [9,10,34].

All the N₂ adsorption-desorption isotherms (Fig. S1E and F) exhibited type IV isotherm with hysteresis loops, which indicated the mesoporous structure of the photocatalysts [8,30]. Compared to the untreated control (36.6 m²/g), higher surface area of the urea treated MnFe₂O₄/g-C₃N₄ (59.4 m²/g) could provide more active sites to improve the adsorption ability and photocatalytic performance of the heterojunction [8,10].

Regardless of urea treatment, the MnFe₂O₄/g-C₃N₄ always displayed a rough surface compared to the uniform decoration of smaller and irregular MnFe₂O₄ nanoparticles and the smooth surface of the pure g-C₃N₄ (Fig. 2; Fig. S2), thus urea treatment did not introduce major morphological changes. All the biophotocathodes were densely and evenly attached with *S. marcescens* as a result of the excellent biocompatibility of MnFe₂O₄ and g-C₃N₄. Element mapping results indicated that the MnFe₂O₄ phase was uniformly distributed throughout the MnFe₂O₄/g-C₃N₄ heterojunction (Fig. S2G-K). The coexistence of C, N, O, Mn and Fe signals in the EDS spectra of the abiotic composite, indicated the successful synthesis of the MnFe₂O₄/g-C₃N₄ photocatalyst. The new signals of Na, K and P on the biotic cathodes was mainly ascribed to the *S. marcescens* Q1 electrophore.

The coexistence of C, N, O, Mn and Fe signals in the MnFe₂O₄/g-C₃N₄ XPS spectra (Fig. S1D) confirmed the successful combination of MnFe₂O₄ and g-C₃N₄, consistent with the XRD results (Fig. 1A), showing

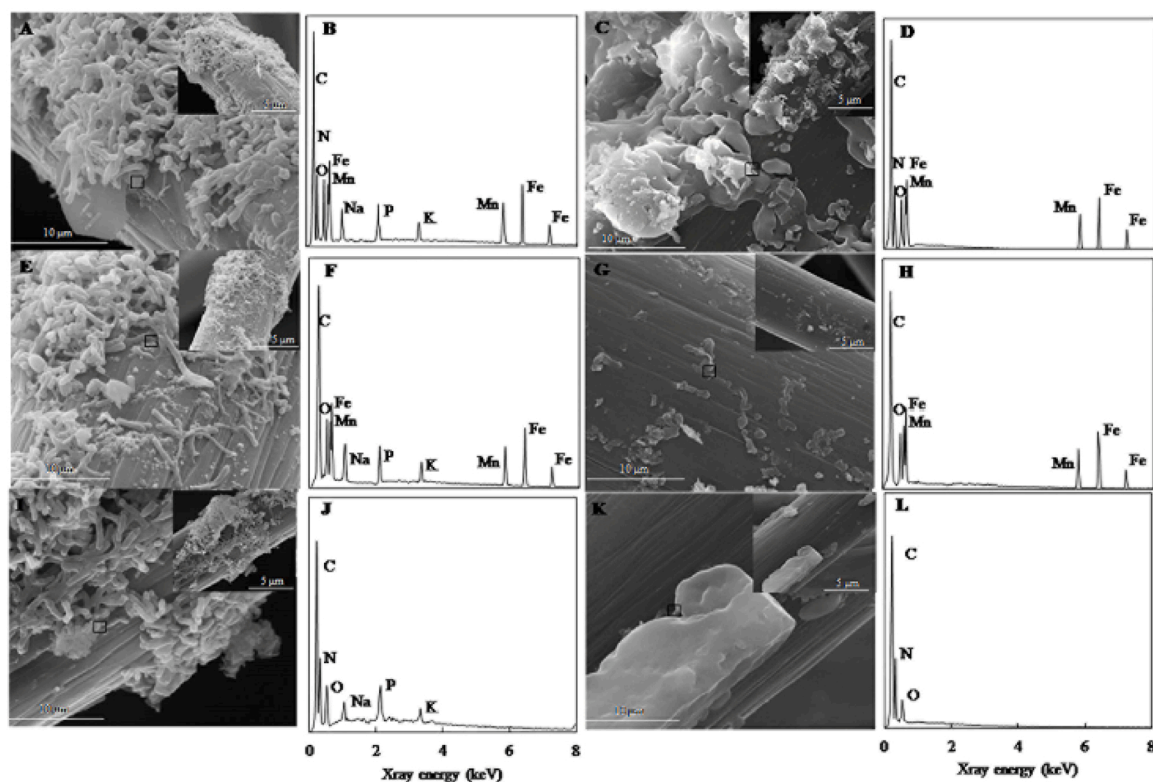


Fig. 2. SEM images on electrodes with urea-treated photocatalysts of $\text{MnFe}_2\text{O}_4/\text{g-C}_3\text{N}_4$ (A and C), MnFe_2O_4 only (E and G), and $\text{g-C}_3\text{N}_4$ only (I and K) with (A, E and I) or without (C, G and K) *S. marcescens*. EDS spectra on the sites of either biotic electrodes (B, F and J) or abiotic electrodes (D, H and L) of $\text{MnFe}_2\text{O}_4/\text{g-C}_3\text{N}_4$ (B and D), MnFe_2O_4 only (F and H) and $\text{g-C}_3\text{N}_4$ only (J and L) (Operational time: 0.5 d).

two peaks at about 641.3 ($\text{Mn } 2p_{3/2}$) and 653.4 eV ($\text{Mn } 2p_{1/2}$) in the Mn 2p spectrum (Fig. 3A) [7,8], along with the two obvious peaks at about 711.3 eV ($\text{Fe } 2p_{3/2}$) and 724.9 eV ($\text{Fe } 2p_{1/2}$) in the Fe 2p spectrum (Fig. 3B) [7], and the two typical peaks at about 284.9 eV ($\text{sp}^2 \text{C-C}$) and 287.9 eV ($\text{sp}^2 \text{N-C=N}$) in the C 1s spectrum (Fig. 3C) [9,10]. Three peaks at about 398.7 eV (pyridinic N), 399.7 eV (pyrrolic N) and 401.3 eV (graphitic N) were exhibited in the N 1s spectrum (Fig. 3D) [21,22]. The significant increase in contents of pyrrolic N after urea treatment, either in $\text{MnFe}_2\text{O}_4/\text{g-C}_3\text{N}_4$ (46.4% vs. 35.2%) or in the single $\text{g-C}_3\text{N}_4$ phase (45.0% vs. 36.1%) (Table 2), indicated changes of N configurations due to urea treatment. Compared to the untreated controls having two peaks at about 530 eV (lattice oxygen) and 532 eV (adsorbed oxygen species), the new broad peak at about 531 eV in O 1s spectra of the urea-treated $\text{MnFe}_2\text{O}_4/\text{g-C}_3\text{N}_4$ or in the single phase MnFe_2O_4 , could be assigned to the oxygen species at the oxygen vacancy sites (Fig. 3E; Table 2) [16,17].

ESR spectroscopy was further employed to demonstrate the presence of oxygen vacancies in the structure of the photocatalysts. A characteristic signal centered at $g = 2.002$, assigned to the electrons trapped in oxygen vacancies [16,17], was displayed in the urea treated $\text{MnFe}_2\text{O}_4/\text{g-C}_3\text{N}_4$ and MnFe_2O_4 only samples (Fig. 3F). The absence of obvious signals in the urea-untreated controls or in the urea treated single-phase $\text{g-C}_3\text{N}_4$, consistent with the XPS results (Fig. 3E; Table 2), further confirmed the occurrence of oxygen vacancies in the MnFe_2O_4 structure.

3.2. MES performance

The impact of urea concentration (Fig. S3), MnFe_2O_4 and $\text{g-C}_3\text{N}_4$ catalysts ratios (Fig. S4) and loading concentrations (Fig. S5) were explored to determine optimal system performance. An urea concentration of 3.28 g/L, a ratio of MnFe_2O_4 and $\text{g-C}_3\text{N}_4$ of 1: 3, and a cathode photocatalyst loading amount of 0.55 mg/cm^2 were thus selected to

achieve the highest photoresponse current, acetate production and CE_{acetate} .

The highest rate of acetate production ($8.5 \pm 0.6 \text{ mM/d}$, Fig. 4A) was obtained with the urea-treated $\text{MnFe}_2\text{O}_4/\text{g-C}_3\text{N}_4$ photocathode incorporating *S. marcescens* at a current density of $5.1 \pm 0.2 \text{ A/m}^2$ (Fig. S6) after 0.5 d operation under illumination, leading to a CE_{acetate} of $96 \pm 3\%$ (Fig. 4D) and an inorganic carbon consumption of $39 \pm 2\%$ (Fig. 4C). These results were remarkably higher than the controls, urea-untreated (acetate: $3.6 \pm 0.3 \text{ mM/d}$, current density: $2.9 \pm 0.2 \text{ A/m}^2$, CE_{acetate} : $71 \pm 4\%$, inorganic carbon consumption: $22 \pm 2\%$), no illumination (acetate: $3.3 \pm 0.3 \text{ mM/d}$, current density: $2.8 \pm 0.2 \text{ A/m}^2$, CE_{acetate} : $67 \pm 3\%$, inorganic carbon consumption: $23 \pm 2\%$), or with urea-treated either only oxygen-vacancy-decorated MnFe_2O_4 (acetate: $2.4 \pm 0.2 \text{ mM/d}$, current density: $2.1 \pm 0.2 \text{ A/m}^2$, CE_{acetate} : $65 \pm 2\%$, inorganic carbon consumption: $19 \pm 2\%$) or only pyrrolic N-enriched $\text{g-C}_3\text{N}_4$ (acetate: $1.9 \pm 0.1 \text{ mM/d}$, current density: $1.9 \pm 0.1 \text{ A/m}^2$, CE_{acetate} : $56 \pm 2\%$, inorganic carbon consumption: $18 \pm 1\%$) in the presence of light (Fig. 4A, C, D; Fig. S6). The efficient acetate production in this photo-assisted MES can be attributed to the synergistic interaction of oxygen vacancies and pyrrolic N. The weak system performance recorded by the urea-untreated photocathodes firmly demonstrated the vital impact of urea treatment for improving the photocatalytic performance. The positive impact of urea treatment on photocatalytic performance has also been reported for $\text{g-C}_3\text{N}_4$ and hydrogen evolution [10], and for BiOBr or $\text{BiOBr/BiOAc}_{1-x}\text{Br}_x$ and Rhodamine B degradation [18,30]. Moreover, compared to the poor values determined with the bare graphite felt cathode, regardless of irradiation (acetate: $1.3 \pm 0.2 \text{ mM/d}$, current density: $1.5 \pm 0.1 \text{ A/m}^2$, CE_{acetate} : $51 \pm 7\%$, inorganic carbon consumption: $14 \pm 1\%$), the performance of all the photocathodes highlighted the positive and essential role of photocatalysts and irradiation in these MES. The detection of H_2 (Fig. 4B) as the sole product at a lower current density (Fig. S6) in the abiotic controls confirmed the essential role of *S. marcescens* in the reduction of

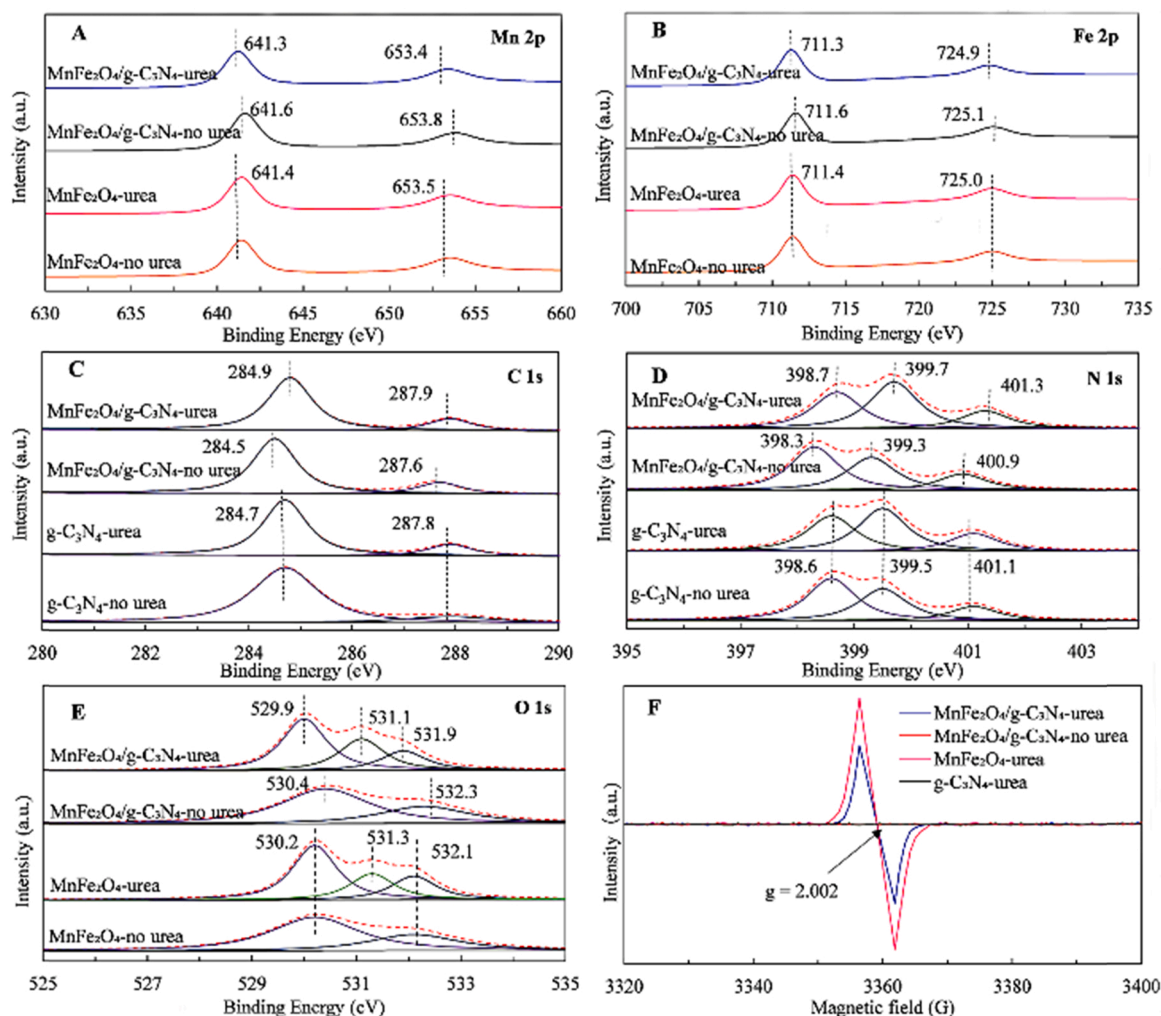


Fig. 3. High resolution XPS spectra of various photocatalysts: Mn 2p (A), Fe 2p (B), C 1s (C), N 1s (D), O 1s (E) and ESR spectra (F).

Table 2

Peak area ratios of different N or O configurations to total area (obtained by XPS spectra).

	N 1s			O 1s		
	Pyridinic nitrogen	Pyrrolic nitrogen	Graphitic nitrogen	Lattice oxygen	Oxygen vacancy	Absorbed oxygen species
MnFe ₂ O ₄ /g-C ₃ N ₄ -urea	36.1% (398.7)	46.4% (399.7)	17.5% (401.3)	50.7% (529.9)	31.0% (531.1)	18.3% (531.9)
MnFe ₂ O ₄ /g-C ₃ N ₄ -no urea	47.7% (398.3)	35.2% (399.3)	17.1% (400.9)	67.6% (530.4)	–	32.4% (532.3)
MnFe ₂ O ₄ -urea	–	–	–	52.8% (530.2)	25.0% (531.3)	22.2% (532.1)
MnFe ₂ O ₄ -no urea	–	–	–	69.7% (530.2)	–	30.3% (532.1)
g-C ₃ N ₄ -urea	36.3% (398.6)	45.0% (399.5)	18.7% (401.1)	–	–	–
g-C ₃ N ₄ -no urea	48.2% (398.6)	36.1% (399.5)	15.7% (401.1)	–	–	–

acetate from inorganic carbon. The production of acetate was directly correlated to the equivalent total H₂ evolution, resulting in lower residual H₂, further confirmed the essential mediation of H₂ in the reduction of inorganic carbon to acetate by the Wood–Ljungdahl pathway [35].

Negligible detrimental effects on the viability of *S. marcescens* based on flow cytometry analysis were observed: 4.1% under illumination, 3.5% without illumination, 1.9% with the bare graphite felt under illumination, 4.9% using the urea-untreated MnFe₂O₄/g-C₃N₄ photocathode and 0.8% without propidium iodide staining (Fig. S7). Similar results were also obtained using the WO₃/MoO₃/g-C₃N₄ [5] or the Ag₃PO₄/g-C₃N₄ [6] photocathode incorporated with the same electro-troph, or the InP photocathode combined with *Methanosarcina barkeri* [1].

These kinetic values were appreciably higher than the previous Ag₃PO₄/g-C₃N₄ (acetate: 5.4 ± 0.1 mM/d, current density: 3.3 ± 0.1 A/m², CE_{acetate}: 93 ± 2%, inorganic carbon consumption: 26 ± 1%) [6] or WO₃/MoO₃/g-C₃N₄ (acetate: 3.1 ± 0.2 mM/d, current density: 2.5 ± 0.3 A/m², CE_{acetate}: 73 ± 4%, inorganic carbon consumption: 20 ± 1%) [5] photocathodes incorporated with the same electro-troph and under same operating conditions. The impact of urea treatment and of the altered charge transfer process can be further appreciated by considering that the urea-untreated MnFe₂O₄/g-C₃N₄ biocathode produced a performance (acetate: 3.6 ± 0.3 mM/d, current density: 2.9 ± 0.2 A/m², CE_{acetate}: 71 ± 4%, inorganic carbon consumption: 22 ± 2%), similar as that obtained using WO₃/MoO₃/g-C₃N₄ (p = 0.300) biocathode, although significantly lower than that using Ag₃PO₄/g-C₃N₄ biocathode. Thus both urea treatment and

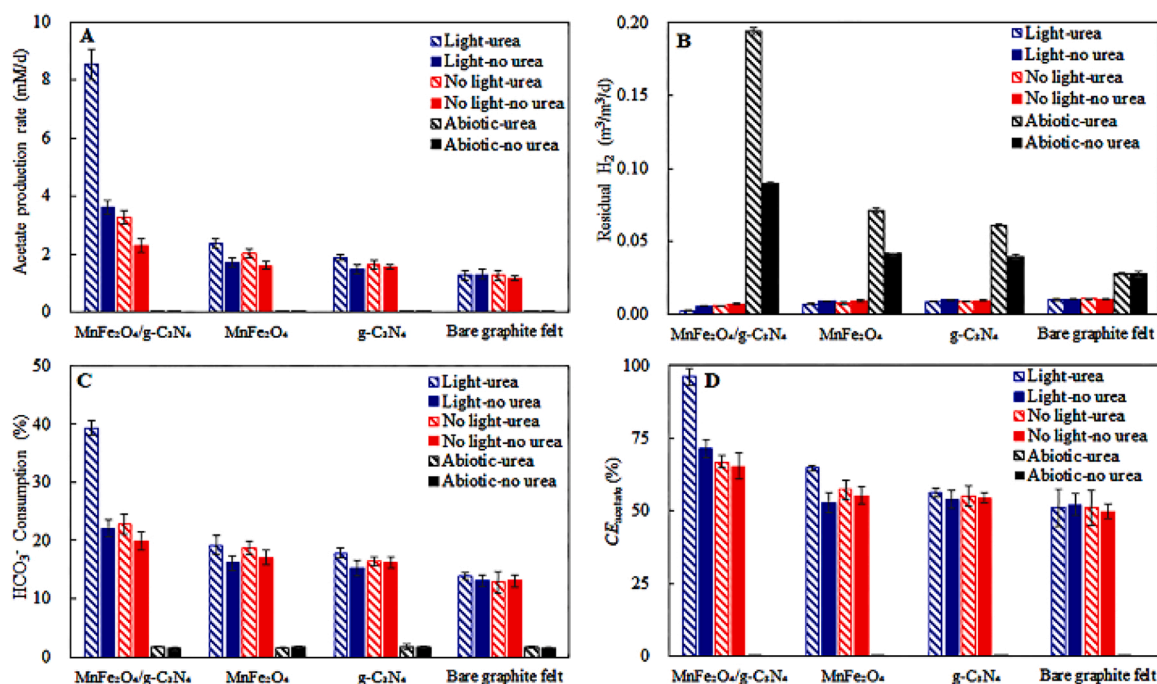


Fig. 4. Comparison of acetate production (A), residual hydrogen (B), inorganic carbon consumption (C), and coulombic efficiency for acetate production (CE_{acetate}) (D) of different cathodes under various conditions (operation time: 0.5 d).

semiconductor selection are important factors determining efficient rates of acetate production. These results were also higher than the reported Si nanowires/TiO₂/Ni photocathode with *Sporomusa ovata* (acetate: 5.0 mM/d, CE_{acetate} : 80%) [4], or the mix-culture ceramic hollow tube wrapped with Ni foam biocathode with a BiVO₄/Mo photoanode (acetate: 0.9 ± 0.2 mM/d, CE_{acetate} : $62 \pm 12\%$) [36].

3.3. Electrochemical analysis

More positive reduction onset potential (-0.31 V) and higher maximum reduction peak current (-2.77 mA) of the biotic treated MnFe₂O₄/g-C₃N₄, compared to the biotic urea-treated MnFe₂O₄ (-0.34 V, -0.82 mA), or g-C₃N₄ (-0.35 V, -0.74 mA), or urea-untreated MnFe₂O₄/g-C₃N₄ (-0.33 V, -1.27 mA) (Fig. 5A; Table S1), clearly proved the more efficient and active catalytic role of the urea-

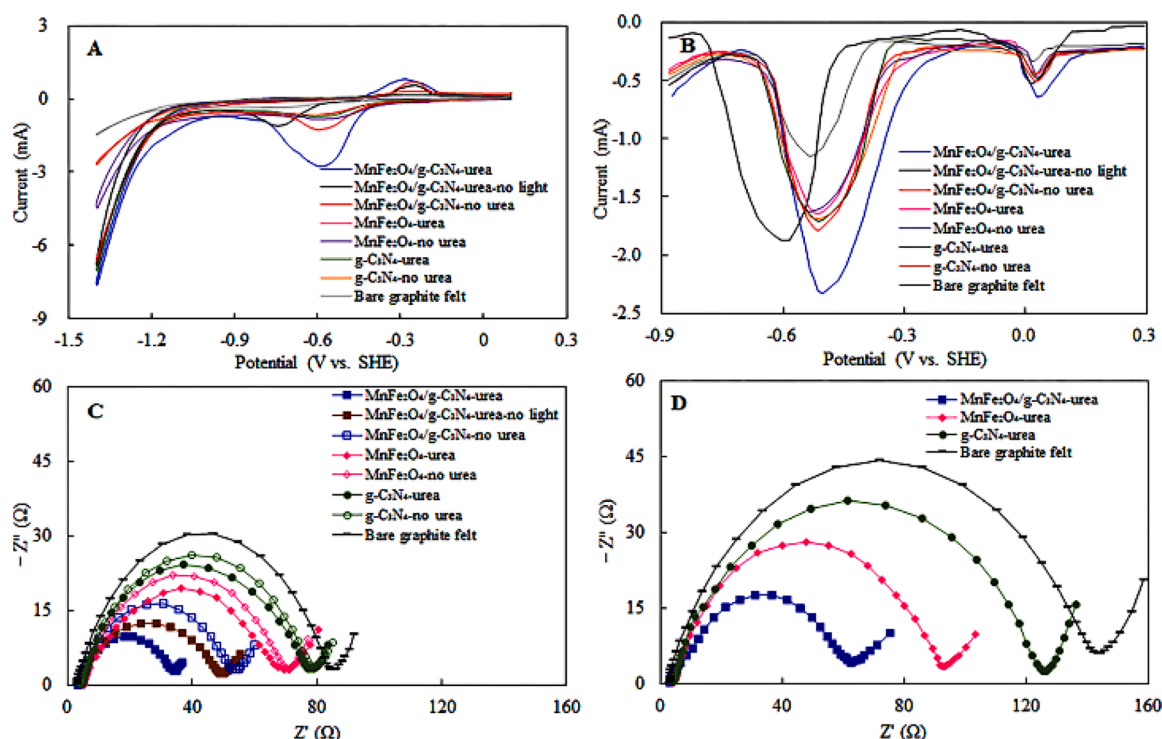


Fig. 5. CVs (A) and DPVs (B) of the biotic cathodes with or without illumination. Nyquist plots of EIS for biotic (C) or abiotic (D) cathodes (operational time: 0.5 d).

treated $\text{MnFe}_2\text{O}_4/\text{g-C}_3\text{N}_4$ by the synergistic effect of oxygen vacancies and pyrrolic nitrogen in inorganic carbon reduction. In addition, the more negative reduction onset potential (-0.44 V) and the lower reduction peak current (-0.36 mA) of the biotic bare graphite felt indicated the vital interaction of photocatalyst and electrotrroph for optimal MES performance, in agreement with the reported Si nanowires and *Sporomusa Ovata* [4], or InP and *Methanosarcina barkeri* [1] for inorganic carbon reduction.

All cathodes exhibited two DPV peaks (Fig. 5B), of which the one at about -0.55 V was similar to the CV (Fig. 5A). The new peak at about 0.02 V was related to outer membrane c-type cytochromes [37,38]. The enhanced catalytic maximum peak current of the urea-treated $\text{MnFe}_2\text{O}_4/\text{g-C}_3\text{N}_4$ (-0.64 mA), compared to the urea-treated single-phases MnFe_2O_4 (-0.46 mA) or $\text{g-C}_3\text{N}_4$ (-0.48 mA), or the urea-untreated $\text{MnFe}_2\text{O}_4/\text{g-C}_3\text{N}_4$ (-0.50 mA) (Fig. 5B; Table S1), inferred the favorable role of pyrrolic N content produced via the urea

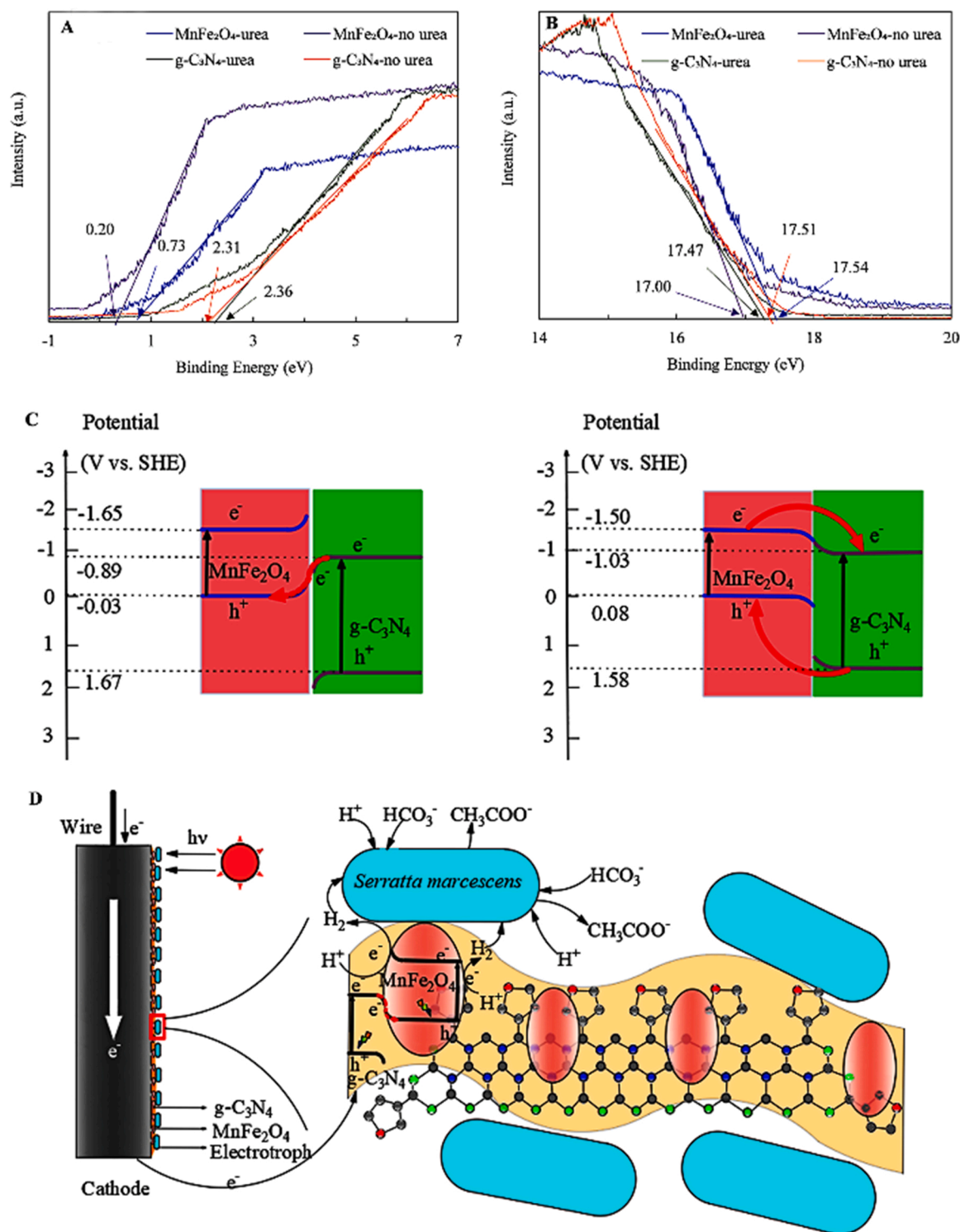


Fig. 6. UPS spectra of various photocatalysts: low (A) and high (B) kinetic energy regions, schematic energy-level diagrams of $\text{MnFe}_2\text{O}_4/\text{g-C}_3\text{N}_4$ heterojunction with (left) or without (right) urea treatment (C), and schematic diagram of the urea-treated $\text{MnFe}_2\text{O}_4/\text{g-C}_3\text{N}_4$ photocathode in the photo-assisted MES (D).

treatment, which favored higher interaction of *c*-type cytochromes and electrodes, thus facilitating extracellular electron transfer. This observation is also supported elsewhere that higher pyrrolic N content in a 3D macroporous N-enriched graphitic carbon scaffold enhanced extracellular electron transfer and thus improved bioelectricity generation in microbial fuel cells [22]. In addition, the lower peak current in the control under darkness, reflected the direct involvement of *c*-type cytochromes in the photocatalytic electrons transfer process, consistent with other hybrid photo-assisted TiO₂ mixed-culture anode of microbial electrolysis cell for enhanced H₂ production via increased current density [39].

The EIS spectra (Fig. 5C and D; Table S1; equivalent circuit (Fig. S8)) demonstrated that charge transfer resistance (R_{ct}) was always dominant over electrolyte resistance (R_s) and diffusion resistance (R_{diff}) with obvious differences. The R_{ct} of urea-treated MnFe₂O₄/g-C₃N₄ (29 Ω) was appreciably lower than the controls (urea-untreated: 45 Ω ; urea-treated MnFe₂O₄ only: 60 Ω ; urea-treated g-C₃N₄ only: 69 Ω ; urea-treated bare graphite felt: 82 Ω) whereas light irradiation significantly reduced R_{ct} , shown as 37 Ω in the controls under darkness. Compared to the abiotic controls (Fig. 5D; Table S1), the biofilms may have provided more active sites for charge transfer, and thus a lower R_{ct} in the biotic photo-assisted MES (Fig. 5C; Table S1).

3.4. Photocatalytic mechanism of MnFe₂O₄/g-C₃N₄ with urea treatment

The direction of interfacial band bending mainly determines the charge transfer mechanism of the heterojunction [28]. Band bending caused by Fermi level (E_F) alignment appears at the heterojunction interface when two different semiconductors form a junction. The one with a higher Fermi level (or higher work function) shows continuously downward band bending whereas the other with a lower Fermi level (or lower work function) exhibits upward band bending [14,29]. The energy levels of different photocatalysts were calculated from UPS (Fig. 6A and B) and UV-vis DRS (Fig. 1E and F) results and summarized in Table 1. For the urea-untreated MnFe₂O₄/g-C₃N₄, since the $E_{F-MnFe_2O_4}$ was higher than the $E_{F-g-C_3N_4}$, the energy bands of MnFe₂O₄ bent downward, while those of g-C₃N₄ bent upward at the interface. The photogenerated charges transfer through a type II mechanism under this band bending structure was illustrated in the right part of Fig. 6C, where photoinduced electrons migrated from the CB of MnFe₂O₄ to that of g-C₃N₄, while the holes at the VB of g-C₃N₄ were injected into that of MnFe₂O₄ according to the band bending direction. The urea-treated MnFe₂O₄/g-C₃N₄ heterojunction also followed the same principle of band bending. A noticeable point was that the $E_{F-g-C_3N_4}$ increased while the $E_{F-MnFe_2O_4}$ decreased after urea treatment. The slightly increased $E_{F-g-C_3N_4}$ was due to the lower electron cloud density of pyrrolic N and higher electronegativity of nitrogen, making it difficult and less likely for electrons to enter the vacuum level [14,40]. Accordingly, the decreased $E_{F-MnFe_2O_4}$ was explained by the appearance of the oxygen vacancies and the subsequent less content of absorbed oxygen species [40–42]. As a consequence, the lower $E_{F-MnFe_2O_4}$ than the $E_{F-g-C_3N_4}$ was ascribed to the synergistic interaction of oxygen vacancies and pyrrolic N, and a reverse band bending direction appeared when the two semiconductors formed a junction. Namely, the energy bands of MnFe₂O₄ bent upward toward the interface, while those of g-C₃N₄ bent downward toward the interface. The type II photogenerated charges transfer thus switched to a Z-scheme mechanism under this circumstance as illustrated in the left part of Fig. 6C, whereas the photogenerated electrons of g-C₃N₄ and photoinduced holes of MnFe₂O₄ recombined at the interface, thereby suppressing the recombination of charge carriers in the same material.

The same conclusions can be also obtained from the binding energy change observed in the XPS results (Fig. 3A–E). The binding energies of Mn 2p, Fe 2p and O 1s of the urea-treated MnFe₂O₄/g-C₃N₄, had slight negative shifts compared to single-phase MnFe₂O₄, whereas the binding energies of C 1s and N 1s showed slight red shifts compared to g-C₃N₄

only. The opposite shift of (C 1s and N 1s) and (Mn 2p, Fe 2p and O 1s) in the urea-treated MnFe₂O₄/g-C₃N₄ indicated the migration of photoinduced electrons from g-C₃N₄ to MnFe₂O₄ following a Z-scheme mechanism [14,31]. The opposite results in the untreated controls, however, suggested that electrons transport occurred from MnFe₂O₄ towards g-C₃N₄ via a type II heterojunction [14,31]. Thus, the photogenerated charge transfer was conclusively switched from type II to a Z-scheme mechanism after urea treatment.

Accordingly, the photocatalytic mechanism of urea-treated MnFe₂O₄/g-C₃N₄ photocathode augmenting the MES of acetate by the electrotroph *S. marcescens* has been summarized in Fig. 6D. Both MnFe₂O₄ and g-C₃N₄ are excited under visible light irradiation, producing photogenerated electrons in the CB and holes in the corresponding VB. According to the band bending direction, the photoinduced electrons of g-C₃N₄ and holes of MnFe₂O₄ recombine at the interface of the heterojunction. Simultaneously, the photogenerated electrons in the CB of MnFe₂O₄ were preserved for H₂ evolution, while the holes in the VB of g-C₃N₄ created a supplementary driving force for trapping the electrons traveling in the external circuit resulting in a higher current generation [5,43]. The remarkable improvement in photocatalytic performance was mainly attributed to the charge transfer switching induced by the synergistic effect of oxygen vacancies and pyrrolic N. Moreover, the increased pyrrolic N facilitated the photo-generated electron transfer from g-C₃N₄ to MnFe₂O₄ [19], leading to the remarkable enhancement of catalytic maximum peak current in CV (Fig. 5A) and DPV (Fig. 5B), as well as the transient photocurrent response (Fig. 1D). In addition, the oxygen vacancies in the MnFe₂O₄ might have exposed a higher number of surface active sites for evolution of H₂ (Fig. 4B) which was subsequently metabolized by the *S. marcescens* Q1 with HCO₃[−] to yield a higher amount of acetate (Fig. 4A) through the Wood–Ljungdahl pathway [6,35].

3.5. Prolonged MES operation with periodical bicarbonate addition

Acetate production (Fig. S9A) and $CE_{acetate}$ (Fig. S9C) predictably decreased after an operational time of 0.5 d due to the insufficient HCO₃[−] supply. The R_{diff} dominated over R_s and R_{ct} , and sharply increased from 52 Ω at 0.5 d to 1074 Ω at 0.75 d (Fig. S9F; Table S2). This phenomenon was caused by the progressive exhaustion of HCO₃[−] with a decrease in the diffusion rate of the reactants in the semi-batch system. Therefore, the R_{diff} sharply climbed to extremely high until subsequent addition of bicarbonate [44]. After each 0.5 d operation, bicarbonate was thus periodically added to maintain an efficient acetate production over 24 days of prolonged continuous operation.

The urea-treated MnFe₂O₄/g-C₃N₄ photocathode accumulated up to 204.4 ± 0.5 mM of acetate (Fig. 7A) (average acetate production rate of 8.5 ± 0.0 mM/d) with an almost unchanged $CE_{acetate}$ of 96 ± 3% (Fig. 7B) over 24 days continuous operation with periodical addition of bicarbonate. The insignificant difference ($p = 0.994$) of the acetate production rates at a 0.5 d operation (8.5 ± 0.6 mM/d, Fig. 4A) and over 24 d (8.5 ± 0.0 mM/d, Fig. 7A) reflected the stability and robustness of the urea-treated MnFe₂O₄/g-C₃N₄ biocathode. These results were significantly higher than the reported 5 mM/d (acetate production) and 80% ($CE_{acetate}$) using a Si nanowires/TiO₂/Ni photocathode over an evidently shorter operation time of 7 days [4]. These values were 3.1-time (acetate production) and 1.7-fold ($CE_{acetate}$) (urea-untreated MnFe₂O₄/g-C₃N₄), 3.6-fold (acetate production) and 1.5-time ($CE_{acetate}$) (MnFe₂O₄ only), 4.6-time (acetate production) and 1.7-fold ($CE_{acetate}$) (sole g-C₃N₄) and 6.6-fold (acetate production) and 1.9-time ($CE_{acetate}$) (bare graphite felt) of the controls (Fig. 7A). Accordingly, a reduced amount of residual H₂, consistent with the higher rate of acetate production in the urea-treated MnFe₂O₄/g-C₃N₄ photocathode (Fig. 7A), was observed relatively to the controls of urea-untreated MnFe₂O₄/g-C₃N₄, MnFe₂O₄ only, g-C₃N₄ only, or bare graphite felt cathodes (Fig. S10A).

The leaching of Mn (1.2 ± 0.4%) and Fe (1.1 ± 0.1%) was essentially

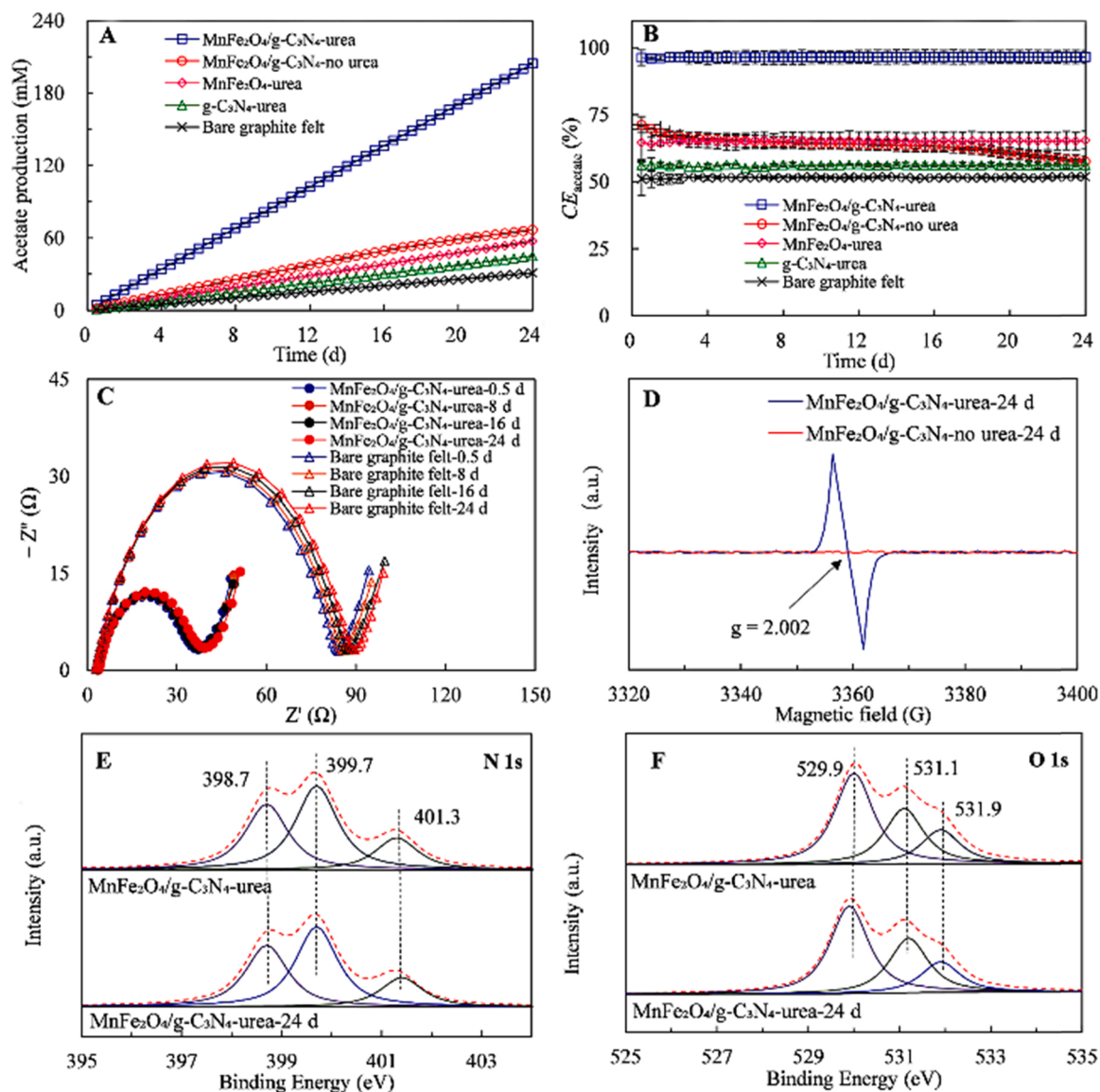


Fig. 7. Acetate production (A), CE_{acetate} (B) over a 24 d operation with periodical addition of bicarbonate. Nyquist plots of EIS (C), ESR spectra (D), high resolution XPS spectra of N 1s (E) and O 1s (F) of $\text{MnFe}_2\text{O}_4/\text{g-C}_3\text{N}_4$ cathode at the end of 24 days operation.

the same and negligible over 24 days operation (Fig. S10B), while the Mn to Fe atom ratio remained at about 1: 2, consistent with the stoichiometric ratio for MnFe_2O_4 . The sharp increase in leaching (Mn: $10.6 \pm 0.7\%$; Fe: $10.4 \pm 0.4\%$) in the urea-untreated controls explained the progressive decline of the urea-untreated $\text{MnFe}_2\text{O}_4/\text{g-C}_3\text{N}_4$ system. Morphology and elementary composition of the urea-treated $\text{MnFe}_2\text{O}_4/\text{g-C}_3\text{N}_4$ after 24 days operation (Fig. S11) was similar as those observed after 0.5 d (Fig. 2). Combining these results with the slight increase in internal resistance (Fig. 7C; Fig. S10C; Table S3) as well as the invariability of the XPS (Fig. 7E and F) and ESR (Fig. 7D) analyses on fresh urea-treated $\text{MnFe}_2\text{O}_4/\text{g-C}_3\text{N}_4$ cathodes and those after 24 days operation, all the experimental evidence forcefully proved the excellent robust stability and durability of the urea-treated $\text{MnFe}_2\text{O}_4/\text{g-C}_3\text{N}_4$ cathode.

4. Conclusions

This study has demonstrated a photo-assisted MES for efficient conversion of inorganic carbon (HCO_3^-) to acetate incorporating an urea-treated $\text{MnFe}_2\text{O}_4/\text{g-C}_3\text{N}_4$ cathode and *S. marcescens* Q1 electro-troph. The MES achieved about 204.4 mM acetate production with a

CE_{acetate} of 96% over 24 days operation with periodical addition of bicarbonate. The outstanding photocatalytic activity of urea-treated $\text{MnFe}_2\text{O}_4/\text{g-C}_3\text{N}_4$ cathode was mainly due to the charge transfer mechanism of the heterojunction which was switched from type II to a Z scheme mechanism by introducing oxygen vacancies and pyrrolic N after urea treatment. The increased pyrrolic N facilitated the photo-generated electrons transfer in the $\text{MnFe}_2\text{O}_4/\text{g-C}_3\text{N}_4$ heterojunction and the oxygen vacancies in the MnFe_2O_4 offered a large fraction of surface active sites, which synergistically contributed to a higher rate of H_2 evolution. The H_2 was subsequently used in-situ by the *S. marcescens* Q1 metabolism with HCO_3^- to produce acetate through the Wood-Ljungdahl pathway. This study demonstrates a simple and feasible method to switch the photocatalytic charge transfer in spinel-based heterojunction via urea treatment and thus provides new insights for highly effective photocatalysts by ingenious synthesis.

CRediT authorship contribution statement

Weifeng Kong: Conceptualization, Methodology, Data curation, Writing – original draft. **Liping Huang:** Conceptualization,

Investigation, Supervision, Validation, Writing – review & editing. **Xie Quan:** Supervision, Writing – review & editing. **Gianluca Li Puma:** Visualization, Writing – review & editing.

Declaration of Competing Interest

There are no conflicts to declare.

Acknowledgements

The National Natural Science Foundation of China (Nos. 52070032 and 21777017), the Fundamental Research Funds for the Central Universities (No. DUT21LAB101), and the Programme of Introducing Talents of Discipline to Universities (B13012) are gratefully acknowledged for financial support.

Appendix A. Supporting information

Supplementary data associated with this article can be found in the online version at [doi:10.1016/j.apcatb.2022.121214](https://doi.org/10.1016/j.apcatb.2022.121214).

References

- [1] E.M. Nichols, J.J. Gallagher, C. Liu, Y. Su, J. Resasco, Y. Yu, Y. Sun, P. Yang, M.C. Y. Chang, C. Chang, Hybrid bioinorganic approach to solar-to-chemical conversion, *Proc. Natl. Acad. Sci. USA* 112 (2015) 11461–11466, <https://doi.org/10.1073/pnas.1508075112>.
- [2] K.K. Sakimoto, S. Zhang, P. Yang, Cysteine-cysteine photoregeneration for oxygenic photosynthesis of acetic acid from CO₂ by a tandem inorganic-biological hybrid system, *Nano Lett.* 16 (2016) 5883–5887, <https://doi.org/10.1021/acs.nanolett.6b02740>.
- [3] S. Cestellos-Blanco, H. Zhang, J.M. Kim, Y.X. Shen, P. Yang, Photosynthetic semiconductor biohybrids for solar-driven biocatalysis, *Nat. Catal.* 45 (2020) 245–255, <https://doi.org/10.1038/s41929-020-0428-y>.
- [4] Y. Su, S. Cestellos-Blanco, J.M. Kim, Y. Shen, Q. Kong, D. Lu, C. Liu, H. Zhang, Y. Cao, P. Yang, Close-packed nanowire-bacteria hybrids for efficient solar-driven CO₂ fixation, *Joule* 4 (2020) 800–811, <https://doi.org/10.1016/j.joule.2020.03.001>.
- [5] Z. Cai, L. Huang, X. Quan, Z. Zhao, Y. Shi, G. Li-Puma, Acetate production from inorganic carbon (HCO₃⁻) in photo-assisted biocathode microbial electrosynthesis systems using WO₃/MoO₃/g-C₃N₄ heterojunctions and *Serratia marcescens* species, *Appl. Catal. B-Environ.* 267 (2020), 118611, <https://doi.org/10.1016/j.apcatb.2020.118611>.
- [6] W. Kong, L. Huang, X. Quan, Z. Zhao, G. Li-Puma, Efficient production of acetate from inorganic carbon (HCO₃⁻) in microbial electrosynthesis systems incorporating Ag₃PO₄/g-C₃N₄ anaerobic photo-assisted biocathodes, *Appl. Catal. B-Environ.* 284 (2021), 119696, <https://doi.org/10.1016/j.apcatb.2020.119696>.
- [7] X. Wang, A. Wang, J. Ma, Visible-light-driven photocatalytic removal of antibiotics by newly designed C₃N₄/MnFe₂O₄-graphene nanocomposites, *J. Hazard. Mater.* 336 (2017) 81–92, <https://doi.org/10.1016/j.jhazmat.2017.04.012>.
- [8] J. Wang, M. Yue, Y. Han, X. Xu, Q. Yue, S. Xu, Highly-efficient degradation of triclosan attributed to peroxymonosulfate activation by heterogeneous catalyst g-C₃N₄/MnFe₂O₄, *Chem. Eng. J.* 391 (2020), 123554, <https://doi.org/10.1016/j.cej.2019.123554>.
- [9] J. Fu, J. Yu, C. Jiang, B. Cheng, g-C₃N₄-Based heterostructured photocatalysts, *Adv. Energy Mater.* 8 (2018), 1701503, <https://doi.org/10.1002/aenm.201701503>.
- [10] V.W.H. Lau, V.W.Z. Yu, F. Ehrat, T. Botari, I. Moudrakovski, T. Simon, V. Duppel, E. Medina, J.K. Stolarczyk, J. Feldmann, V. Blum, B.V. Lotsch, Urea-modified carbon nitrides: enhancing photocatalytic hydrogen evolution by rational defect engineering, *Adv. Energy Mater.* 7 (2017), 1602251, <https://doi.org/10.1002/aenm.201602251>.
- [11] K. Vignesh, A. Suganthi, B.K. Min, M. Kang, Photocatalytic activity of magnetically recoverable MnFe₂O₄/g-C₃N₄/TiO₂ nanocomposite under simulated solar light irradiation, *J. Mol. Catal. A-Chem.* 395 (2014) 373–383, <https://doi.org/10.1016/j.molcata.2014.08.040>.
- [12] X. Yang, L. Tian, X. Zhao, H. Tang, Q. Liu, G. Li, Interfacial optimization of g-C₃N₄-based Z-scheme heterojunction toward synergistic enhancement of solar-driven photocatalytic oxygen evolution, *Appl. Catal. B-Environ.* 244 (2019) 240–249, <https://doi.org/10.1016/j.apcatb.2018.11.056>.
- [13] W.K. Jo, N.C.S. Selvam, Z-scheme CdS/g-C₃N₄ composites with RGO as an electron mediator for efficient photocatalytic H₂ production and pollutant degradation, *Chem. Eng. J.* 317 (2017) 913–924, <https://doi.org/10.1016/j.cej.2017.02.129>.
- [14] Z. Huang, J. Song, X. Wang, L. Pan, K. Li, X. Zhang, L. Wang, J. Zou, Switching charge transfer of C₃N₄/W₁₈O₄₉ from type-II to Z-scheme by interfacial band bending for highly efficient photocatalytic hydrogen evolution, *Nano Energy* 40 (2017) 308–316, <https://doi.org/10.1016/j.nanoen.2017.08.032>.
- [15] S. Xiao, Q. Fu, Z. Li, J. Li, L. Zhang, Q. Liao, Solar-driven biological inorganic hybrid systems for the production of solar fuels and chemicals from carbon dioxide, *Renew. Sust. Energy Rev.* 150 (2021), 111375, <https://doi.org/10.1016/j.rser.2021.111375>.
- [16] S. Chen, H. Wang, Z. Kang, S. Jin, X. Zhang, X. Zheng, Z. Qi, J. Zhu, B. Pan, Y. Xie, Oxygen vacancy associated single-electron transfer for photofixation of CO₂ to long-chain chemicals, *Nat. Commun.* 10 (2019) 788, <https://doi.org/10.1038/s41467-019-08697-x>.
- [17] L. Liang, X. Li, Y. Sun, Y. Tan, X. Jiao, H. Ju, Z. Qi, J. Zhu, Y. Xie, Infrared light-driven CO₂ overall splitting at room temperature, *Joule* 2 (2018) 1004–1016, <https://doi.org/10.1016/j.joule.2018.02.019>.
- [18] M. Song, M. Du, Q. Liu, F. Xing, C. Huang, X. Qiu, Enhancement of photocatalytic activities in hierarchical BiOBr microflowers induced by oxygen vacancies, *Catal. Today* 335 (2019) 193–199, <https://doi.org/10.1016/j.cattod.2018.11.006>.
- [19] Y. Xu, Y. Mo, J. Tian, P. Wang, H. Yu, J. Yu, The synergistic effect of graphitic N and pyrrolic N for the enhanced photocatalytic performance of nitrogen-doped graphene/TiO₂ nanocomposites, *Appl. Catal. B-Environ.* 181 (2016) 810–817, <https://doi.org/10.1016/j.apcatb.2015.08.049>.
- [20] R. Shi, Z. Li, H. Yu, L. Shang, C. Zhou, G.I.N. Waterhouse, L. Wu, T. Zhang, Effect of nitrogen doping level on the performance of N-doped carbon quantum dot/TiO₂ composites for photocatalytic hydrogen evolution, *ChemSusChem* 10 (2017) 4650–4656, <https://doi.org/10.1002/cssc.201700943>.
- [21] X. Liu, X. Sun, J. Chen, Y. Huang, J. Xie, W. Li, G. Sheng, Y. Zhang, F. Zhao, R. Lu, H. Yu, Phenothiazine derivative-accelerated microbial extracellular electron transfer in bioelectrochemical system, *Sci. Rep.* 3 (2013) 1616, <https://doi.org/10.1038/srep01616>.
- [22] S. You, M. Ma, W. Wang, D. Qi, X. Chen, J. Qu, N. Ren, 3D Macroporous nitrogen-enriched graphitic carbon scaffold for efficient bioelectricity generation in microbial fuel cells, *Adv. Energy Mater.* 7 (2017), 1601364, <https://doi.org/10.1002/aenm.201601364>.
- [23] L. Huang, L. Gan, N. Wang, X. Quan, B.E. Logan, G. Chen, Mineralization of pentachlorophenol with enhanced degradation and power generation from air cathode microbial fuel cells, *Biotechnol. Bioeng.* 109 (2012) 2211–2221, <https://doi.org/10.1002/bit.24489>.
- [24] Y. Chen, J. Shen, L. Huang, Y. Pan, X. Quan, Enhanced Cd(II) removal with simultaneous hydrogen production in biocathode microbial electrolysis cells in the presence of acetate or NaHCO₃, *Inter. J. Hydrogen Energy* 41 (2016) 13368–13379, <https://doi.org/10.1016/j.ijhydene.2016.06.200>.
- [25] Q. Wang, L. Huang, Y. Pan, P. Zhou, X. Quan, B.E. Logan, H. Chen, Cooperative cathode electrode and in situ deposited copper for subsequent enhanced Cd(II) removal and hydrogen evolution in bioelectrochemical systems, *Bioresour. Technol.* 200 (2016) 565–571, <https://doi.org/10.1002/cssc.201100604>.
- [26] Q. Wang, L. Huang, X. Quan, G. Li-Puma, Sequential anaerobic and electro-Fenton processes mediated by W and Mo oxides for degradation/mineralization of azo dye methyl orange in photo assisted microbial fuel cells, *Appl. Catal. B-Environ.* 245 (2019) 672–680, <https://doi.org/10.1016/j.apcatb.2019.01.026>.
- [27] L. Huang, Y. Liu, L. Yu, X. Quan, G. Chen, A new clean approach for production of cobalt dihydroxide from aqueous Co(II) using oxygen-reducing biocathode microbial fuel cells, *J. Clean. Prod.* 86 (2015) 441–446, <https://doi.org/10.1016/j.jclepro.2014.08.018>.
- [28] J. Liu, Y. Liu, N. Liu, Y. Han, X. Zhang, H. Huang, Y. Lifshitz, S.T. Lee, J. Zhong, Z. Kang, Metal-free efficient photocatalyst for stable visible water splitting via a two-electron pathway, *Science* 347 (2015) 970–974, <https://doi.org/10.1126/science.aaa3145>.
- [29] M.E. Aguirre, R. Zhou, A.J. Eugene, M.I. Guzman, M.A. Grela, Cu₂O/TiO₂ heterostructures for CO₂ reduction through a direct Z-scheme: Protecting Cu₂O from photocorrosion, *Appl. Catal. B-Environ.* 217 (2017) 485–493, <https://doi.org/10.1016/j.apcatb.2017.05.058>.
- [30] X. Jia, Q. Han, H. Liu, S. Li, H. Bi, A dual strategy to construct flowerlike S-scheme BiOBr/BiOAc_{1-x}Br_x heterojunction with enhanced visible-light photocatalytic activity, *Chem. Eng. J.* 399 (2020), 125701, <https://doi.org/10.1016/j.cej.2020.125701>.
- [31] W. Chang, W. Xue, E. Liu, J. Fan, B. Zhao, Highly efficient H₂ production over NiCo₂O₄ decorated g-C₃N₄ by photocatalytic water reduction, *Chem. Eng. J.* 362 (2019) 392–401, <https://doi.org/10.1016/j.cej.2019.01.021>.
- [32] J. Tauc, Optical properties and electronic structure of amorphous, *Mater. Res. Bull.* 3 (1968) 37, [https://doi.org/10.1016/0025-5408\(68\)90023-8](https://doi.org/10.1016/0025-5408(68)90023-8).
- [33] F. Meng, J. Li, S.K. Cushing, M. Zhi, N. Wu, Solar hydrogen generation by nanoscale p-n junction of p-type molybdenum disulfide/n-type nitrogen-doped reduced graphene oxide, *J. Am. Chem. Soc.* 135 (2013) 10286–10289, <https://doi.org/10.1021/ja404851s>.
- [34] S. Wu, X. Tan, J. Lei, H. Chen, L. Wang, J. Zhang, Ga-doped and Pt-loaded porous TiO₂-SiO₂ for photocatalytic nonoxidative coupling of methane, *J. Am. Chem. Soc.* 141 (2019) 6592–6600, <https://doi.org/10.1021/jacs.8b13858>.
- [35] E. Blanchet, F. Duquenne, Y. Raftai, L. Etcheverry, B. Erable, A. Bergel, Importance of the hydrogen route in up-scaling electrosynthesis for microbial CO₂ reduction, *Energy Environ. Sci.* 8 (2015) 3731–3744, <https://doi.org/10.1039/C5TA05503B>.
- [36] B. Bian, L. Shi, K.P. Katuri, J. Xu, P. Wang, P.E. Saikaly, Efficient solar-to-acetate conversion from CO₂ through microbial electrosynthesis coupled with stable photoanode, *Appl. Energy* 278 (2020), 115684, <https://doi.org/10.1016/j.apenergy.2020.115684>.
- [37] Y. Xiao, E. Zhang, J. Zhang, Y. Dai, Z. Yang, H.E.M. Christensen, J. Ulstrup, F. Zhao, Extracellular polymeric substances are transient media for microbial extracellular electron transfer, *Sci. Adv.* 3 (2017), e1700623, <https://doi.org/10.1126/sciadv.1700623>.
- [38] K. Sathishkumar, Y. Li, E. Sanganyado, Electrochemical behavior of biochar and its effects on microbial nitrate reduction: Role of extracellular polymeric substances in

- extracellular electron transfer, *Chem. Eng. J.* 395 (2020), 125077, <https://doi.org/10.1016/j.cej.2020.125077>.
- [39] D. Zhou, S. Dong, D. Ki, B.E. Rittmann, Photocatalytic-induced electron transfer via anode-respiring bacteria (ARB) at an anode that intimately couples ARB and a TiO₂ photocatalyst, *Chem. Eng. J.* 338 (2018) 745–751, <https://doi.org/10.1016/j.cej.2018.01.094>.
- [40] Z. Zhang, J.T. Yates, Band bending in semiconductors: chemical and physical consequences at surfaces and interfaces, *Chem. Rev.* 112 (2012) 5520–5551, <https://doi.org/10.1021/cr3000626>.
- [41] H. Chen, Y. Zhao, L. Shi, G. Li, L. Sun, X. Zou, Revealing the relationship between energy level and gas sensing performance in heteroatom-doped semiconducting nanostructures, *Appl. Mater. Interfaces* 10 (2018) 29795–29804, <https://doi.org/10.1021/acsami.8b10057>.
- [42] D. Meggiolaro, E. Mosconi, F. De Angelis, Modeling the interaction of molecular iodine with MAPbI₃: a probe of lead-halide perovskites defect chemistry, *ACS Energy Lett.* 3 (2018) 447–451, <https://doi.org/10.1021/acsenenergylett.7b01244>.
- [43] Y. Hou, Y. Gan, Z. Yu, X. Chen, L. Qian, B. Zhang, L. Huang, J. Huang, Solar promoted azo dye degradation and energy production in the bio-photoelectrochemical system with a g-C₃N₄/BiOBr heterojunction photocathode, *J. Power Sources* 371 (2017) 26–34, <https://doi.org/10.1016/j.jpowsour.2017.10.033>.
- [44] G. Mohanakrishna, K. Vanbroekhoven, D. Pant, Impact of dissolved carbon dioxide concentration on the process parameters during its conversion to acetate through microbial electrosynthesis, *React. Chem. Eng.* 3 (2018) 371–378, <https://doi.org/10.1039/C7RE00220C>.